



# Numerical Flow Simulation and Cavitation Prediction in a Centrifugal Pump using an SST-SAS Turbulence Model

M. Ennouri<sup>†</sup>, H. Kanfoudi, A. Bel Hadj Taher and R. Zgolli

*Laboratory of Hydraulic and Environment Modeling, National Engineering School of Tunis, University of Tunis El Manar, Tunis, 1002, Tunisia*

<sup>†</sup>Corresponding Author Email: [marwa.ennouri@enit.utm.tn](mailto:marwa.ennouri@enit.utm.tn)

(Received January 8, 2018; accepted July 24, 2018)

## ABSTRACT

The paper handles the subject of the modelling and simulation of the flow inside a centrifugal pump through non-cavitating and cavitating conditions. Operating under cavitation state is so perilous to a pump and can considerably reduce its lifetime service. Hence, to provide highly reliable pumps, it is essential to comprehend the inner flow of pumps. The investigated centrifugal pump comprises five backward curved-bladed impeller running at 900 rpm. The modelling process started with an unsteady numerical analysis under non-cavitating conditions to validate the numerical model and the solver comparing with the available testing data. Due to high Reynolds numbers, turbulence effects have been taken into account by unsteady RANS methods using an SST-SAS turbulence model. The obtained pump performances were numerically compared with the experimental ones, and the outcome shows an acceptable agreement between both. The temporal distribution of the internal flow parameters such as pressure and velocity was then studied. Furthermore, basic investigations of cavitating flow around 3D NACA66-MOD profile using a recently developed and validate cavitation model was established. The verification of the numerical simulation validity was based on comparing calculated and experimental results and presented good agreement. Finally, a 3D simulation of the inception of the cavitating pocket inside the centrifugal pump is performed to analyze the impact of the cavitation in the decrease of the head and efficiency.

**Keywords:** Unsteady simulation; Scale-adaptive simulation; NACA66; Centrifugal pump; Cavitation.

## NOMENCLATURE

$b_1$	inlet impeller width	$R_3$	base volute radius
$b_2$	outlet impeller width	$t$	time
$b_3$	volute width	$t_{ref}$	one impeller rotation
$c$	hydrofoil chord	$t_{BP}$	the blade-passing time
$C_L$	the coefficient of lift	$U_\infty$	velocity
$C_D$	the coefficient of drag	$u_2$	peripheral velocity at impeller outlet
$d_2$	outlet impeller diameter	$\alpha$	vapour volume fraction
$e$	blade thickness	$\beta_1$	inlet blade angle
$g$	gravity	$\beta_2$	outlet blade angle
$H$	total head	$\theta_1$	blade LE inclination angle
$N_a$	blade number	$\theta_2$	blade Te inclination angle
$P$	pressure	$\rho$	density
$P^*$	$=P-P_{ave}$	$\sigma$	the cavitation number
$P_{adim}$	$=P/0.5 \cdot \rho \cdot u_2^2$	$\Phi$	flow coefficient
$Q, Q_N$	flow rate, nominal flow rate	$\psi$	head coefficient
$R_i$	inlet flange radius	$\omega$	rotating speed
$R_1$	mean impeller inlet radius		
$R_2$	mean impeller outlet radius		

## 1. INTRODUCTION

Centrifugal pumps are undoubtedly among the main commonly used machinery in the field of industry as well as domestic applications. Compared to oldest kinds of centrifugal pumps, the new generation produces higher efficiency. This is why, in today's energy aware and extremely competing world, the prominence has been accorded on developing pumps with higher efficiency. In fact, every efficiency percentage gained can ensure important energy saving over the length of service of the turbomachines. Therefore, a further consideration about the physics and the flow field within the pump is still required in order to improve the pump performance. For this reason, a great scientific interest is granted for this type of hydraulic machine. For a detailed understanding of the internal flow, numerous experiments have been conducted (Dong and Katz 1995; Dong, Chu, and Katz 1997; Akhras *et al.* 2004; Tan *et al.* 2012).

In order to have the best cost-effective design and before the production, it is essential to predict the performance of the pumps in advance, except that it is a lengthy and pricey process.

As an alternative, the Computational Fluid Dynamics (CFD) tools are able to study precisely the internal flow in complex geometries like the centrifugal pumps. They are a combination of applied mathematics, physics and computational software. These tools allow, on the one hand, to visualize how a liquid circulates and, on the other hand, how it affects objects as it passes (Maxime and Li 2016). Thanks to the expansion of CFD codes and the growing availability of computer power, researchers actually prefer this method.

According to the investigation lead by (Yulin, Shuhong, and Jie 2009), the unsteady obtained results revealed to be reliable in forecasting the flow behaviour in the centrifugal model pump. In fact, their comparison with the experimental data gained by PIV measurement presents good agreement.

The relative movement between impeller and volute produces an unsteady interaction, which generates not only pressure fluctuations but also influences the overall pump performance. This is a direct consequence of the three-dimensionality and the complexity of the flow field inside a centrifugal pump, not to mention the fact that it is extremely turbulent. Pressure fluctuations induce unsteady forces over the mechanical components, which are one of the main sources of hydraulic noise and vibration.

Starting from the works of (Croba and Kueny 1996; Kitano and H.E 2000; Bakir *et al.* 2001; Parrondogayo, Gonzalez-Perez, and Fernandez-Francos 2002) up to today, many studies have been done on the impeller-volute interaction and pressure fluctuation characteristics by numerical or experimental methods which offer a valuable references (Akhras *et al.* 2004; Asuaje *et al.* 2005; Majidi 2005; González and Santolaria 2006; Cheah, Lee, and Winoto 2008; Feng, Benra, and Dohmen 2009;

Barrio, Parrondo, and Blanco 2010; Li *et al.* 2013; Longatte and Kueny 1999; Shuai *et al.* 2015; Al-Qtub, Khalifa, and Khulief 2009; Pavesi, Cavazzini, and Ardizzone 2008; Zhang *et al.* 2015).

The importance given to the pressure fluctuations lies in the fact that it constitutes the source inducing the onset of the phenomenon of cavitation. It is one of the main problems that hamper the hydraulic machinery performances. Cavitation induces pressure fluctuation and irregular load distribution, and then reduce noticeably the efficiency of pumps and affect their operational stability. The related noise and vibrations, as well as cavitation erosion, reduce the service life of centrifugal pumps (Brennen 2011).

Many approaches, for the simulation of the cavitating flow, have been established during the recent years and a great number of mathematical formulations have received increasing attention, particularly the homogeneous flow models (Sauer and Schnerr 2000; Yuan, Sauer, and Schnerr 2001; Kubota, Kato, and Yamaguchi 1992; Koop 2008; Kozubková, Rautová, and Bojko 2012), (Zwart, Gerber, and Belamri 2004) and (Kanfoudi and Zgolli 2011; Kanfoudi and Zgolli 2011 Kanfoudi, Lamloumi, and Zgolli 2012, 2014; Kanfoudi 2015). This technique is commonly divided into two types based on how to find out the mixture density as the Barotropic equation models (BEM) and the Transport equation based models (TEM).

The pressure variation of a fluid is related to their density through a barotropic state law which constitutes the BEM base (Deshpande, Feng, and Merkle 1994; Laberteaux and Ceccio 2001; Coutier-Delgosha, Reboud, and Dellanoy 2003; Coutier-Delgosha *et al.* 2005; Pouffay *et al.* 2005; Barre *et al.* 2009). Many authors proposed in literature numerous sources terms of TEM (Sauer and Schnerr 2000; Singhal *et al.* 2002; Senocak and Shyy 2004; Zwart, Gerber, and Belamri 2004; Kanfoudi and Zgolli 2011) and many of them are applied on turbomachinery. For instance, (Liu *et al.* 2014; Meng *et al.* 2014; Xu *et al.* 2014; Hosono *et al.* 2015; Song *et al.* 2015; Meng *et al.* 2016; Tan 2016) used the model developed by (Zwart, Gerber, and Belamri 2004); (Liu *et al.* 2013; Maxime and Li 2016) tested the cavitation model proposed by (Sauer and Schnerr 2000). The full cavitation model (Singhal *et al.* 2002) which is also a TEM, was tried by (Lei *et al.* 2013; Lei *et al.* 2013; Li 2014). Initially applied to the centrifugal pump by (Lamloumi, Kanfoudi, and Zgolli 2012), the (Kanfoudi and Zgolli 2011) cavitation model, is considered in the present paper.

A precise prediction of the cavitating flow field is to accurately determine the turbulent quantities. Consequently, the turbulence model adopted should be very appropriate and satisfy the condition mentioned above. Indeed, (Wu, Utturkar, and Shyy 2003; Wu, Wang, and Shyy 2005; Shojaeefard *et al.* 2013) revealed lately that the modelling of turbulence had a serious consequence on the simulation of the unsteady cavitating flow.

A more promising method denoted as the hybrid approach is used. It combines the advantages of RANS

and large eddy simulation LES. Indeed, it increases potentially the computational efficiency like the LES approach and it is more accurate than the RANS. (Menter and Egorov 2010) suggested the SST Scale-Adaptive Simulation (SST-SAS). This turbulence model was validated on several generic examples and more complex industrial-type applications (Winkler and Dorgan 2011; Wang and Li 2014). Capable of capturing successfully the features of cavitating flows, like the re-entrant jet considered as the leading factor responsible for the cavity shedding (Lauder and Spalding 1974), the SST-SAS turbulence model is used in the present paper.

Focusing on the modelling and simulation of the appearance of cavitation in a radial pump on the one hand and trying to predict the impact of this phenomenon on the performance of the machine, on the other hand, this work will include the details of the numerical techniques employed. This article is a set of three principal parts. The first one deals with a numerical study of a centrifugal pump considering the whole 3D geometry and the unsteadiness of the flow on non-cavitating conditions. The calculated pump performances are then used to validate the numerical model and the solver. This is done by comparing the obtained numerical results with the available data (Kergourlay *et al.* 2007). The temporal distribution of the flow parameters are then identified, the internal complex flow behaviour is studied, and the effect of the blade-tongue interaction can be easily investigated.

The second part of the paper focuses on the validation of the cavitation model adopted (Kanfoudi and Zgolli 2011), over a 3D NACA66-MOD hydrofoil. The experimental results of (Leroux, Astolfi, and Billard 2004) are used to validate the numerical simulation

The last part describes the application of the new cavitation model to simulate the internal hydrodynamics of the centrifugal pump (Ns32) in cavitating conditions. This is done for the purpose to predict the inception of the vapour, the head drop behaviour and the impact on its efficiency. The observations of the pump performance led us to carry out a detailed analysis of the stability and accuracy of our proposed model and the influence of cavitation in a complex rotating geometry.

## 2. MATHEMATICAL FORMULATIONS AND NUMERICAL METHOD

### 2.1 Governing Equations and Turbulence Model

Both the liquid and vapour phases, in addition to the phase transition mechanism between the two, are illustrated in the problem.

A single-fluid (mixture) is taken into account and presented through the local vapour volume fraction.

The one fluid share the same spatial and temporal variation of the vapour fraction, which is defined through a transport equation comprising source terms for the mass transfer rate between the phases.

The numerical analysis is performed using the SST Scale-Adaptive Simulation to solve the unsteady Reynolds-averaged Navier–Stokes (RANS). In the mixture model, the multiphase fluid components are supposed to have the same velocity and pressure. The RANS model (equation: (1) Continuity and (2) momentum) is coupled with a mass transfer cavitation model.

$$\frac{\partial \rho_m}{\partial t} + \frac{\partial(\rho_m u_j)}{\partial x_j} = 0 \quad (1)$$

$$\frac{\partial(\rho_m u_i)}{\partial t} + \frac{\partial(\rho_m u_i u_j)}{\partial x_j} = \rho_m f_i - \frac{\partial P}{\partial x_j} + \frac{\partial}{\partial x_j} \left[ (\mu + \mu_t) \left( \frac{\partial u_i}{\partial x_j} + \frac{\partial u_j}{\partial x_i} - \frac{2}{3} \frac{\partial u_k}{\partial x_k} \delta_{ij} \right) \right] + B \quad (2)$$

With:

$$B = -\rho_m \omega u_i + \rho_m \omega (\omega r) \quad (3)$$

Where:  $u_i$  the velocity,  $P$  is the pressure, Coriolis forces and centrifugal forces are added as a dynamic source term (term  $B$ ),  $\mu$  and  $\mu_t$  are the laminar viscosity and the turbulent viscosity respectively and  $\rho_m$  is the density.

The effective density and viscosity of the mixture are respectively given by:

$$\begin{aligned} \rho_m &= \alpha_v \rho_\alpha + (1 - \alpha_v) \rho_l ; \\ \mu_m &= \alpha_v \mu_\alpha + (1 - \alpha_v) \mu_l \end{aligned} \quad (4)$$

Where:  $\alpha_v$  is the vapor fraction ( $\alpha_v = 1$ : vapor and for  $\alpha_v = 0$ : liquid). The density and the viscosity of liquid and vapour are presumed to be a constant model.

The eddy-viscosity is calculated according to:

$$\mu_t = \frac{\rho_m a k}{\max(a\omega, S F_2)} \quad (5)$$

The value  $a$  is set to 0.31,  $F_2$  is a blending function which restricts the limiter to the wall boundary,  $S$  is an invariant measure of the strain rate, more details can be found in (Menter 1994)

Two supplementary transport equations are solved, one for the turbulent kinetic energy  $k$  and one for the turbulent frequency  $\omega$ :

$$\begin{aligned} \frac{\partial \rho k}{\partial t} + \frac{\partial}{\partial x_j} (\rho U_j k) &= P_k - \rho c_\mu k \omega \\ &+ \frac{\partial}{\partial x_j} \left[ \left( \mu + \frac{\mu_t}{\sigma_k} \right) \frac{\partial k}{\partial x_j} \right] \end{aligned} \quad (6)$$

$$\begin{aligned} \frac{\partial \rho \omega}{\partial t} + \frac{\partial}{\partial x_j} (\rho U_j \omega) &= \alpha \frac{\omega}{k} P_k - \rho \beta \omega^2 + Q_{SAS} \\ &+ \frac{\partial}{\partial x_j} \left[ \left( \mu + \frac{\mu_t}{\sigma_\omega} \right) \frac{\partial \omega}{\partial x_j} \right] + (1 + F_1) \frac{2\rho}{\sigma_{\omega 2}} \frac{1}{\omega} \frac{\partial k}{\partial x_j} \frac{\partial \omega}{\partial x_j} \end{aligned} \quad (7)$$

where  $\sigma_{\omega 2}$  is the value for the  $k$ - $\varepsilon$  regime of the SST model (Menter 1994).

The additional source term  $Q_{SAS}$ , added to the right-hand side of the SST  $\omega$ -equation, will calibrate the high wave number damping to resolve turbulence structure at the high wave number end of the spectrum (Menter and Egorov 2010). The expression of this term:

$$Q_{SAS} = \max \left[ \begin{array}{l} \rho \xi_2 \kappa S^2 \left( \frac{L}{L_{vK}} \right)^2 - \\ C_{SAS} \frac{2\rho k}{\sigma_\phi} \max \left( \frac{1}{\omega^2} \frac{\partial \omega}{\partial x_j} \frac{\partial \omega}{\partial x_j}, \frac{1}{k^2} \frac{\partial k}{\partial x_j} \frac{\partial k}{\partial x_j} \right), 0 \end{array} \right] \quad (8)$$

With  $\xi_2=1.47$ ,  $\sigma_\phi=2/3$  and  $C_{SAS}=2$  and:

$$L_{vK} = \kappa \left| \frac{U'}{U''} \right|; \quad L = c_\mu^{-1/4} \frac{\sqrt{k}}{\omega}; \quad (9)$$

$$U'' = \sqrt{\frac{\partial^2 U_i}{\partial x_k^2} \frac{\partial^2 U_i}{\partial x_j^2}}; \quad U' = \sqrt{2 \cdot S_{ij} S_{ij}}$$

Furthermore, in order to avoid accumulation of energy, a high wave number damping is used in the model, at the smallest scales. This is accomplished by setting a lower limit of the von Karman length scale:

$$L_{vK} = \max \left( \kappa \left| \frac{U'}{U''} \right|; C_s \sqrt{\frac{\kappa \xi_2}{\beta/c_\mu - \alpha}} \Delta \right); \quad (10)$$

$$\Delta = \sqrt[3]{V}$$

With  $C_s = 0.11$ ,  $K=0.41$ ,  $C_\mu=0.09$  and  $\alpha=0.44$ ,  $\beta=0.0828$  are the  $k$ - $\varepsilon$  related coefficients of the SST model (Menter and Egorov 2010).

By adding this source term to the transport equation of the turbulent frequency, the Scale-Adaptive Simulation (SAS) is an improved URANS formulation. This correction allows the resolution of the turbulent spectrum in unstable flow conditions and simulates the detachment of the cavitation pocket.

To reproduce the same behaviour of the LES in unstable flow region, the SST-SAS is based on the addition of the von Karman length-scale.

## 2.2 Physical Cavitation Model

The development of the cavitation phenomenon is governed by the subsequent mass transfer equation:

$$\frac{\partial(\rho_v \alpha_v)}{\partial t} + \frac{\partial(\rho_v \alpha_v u_i)}{\partial x_i} = m^+ - m^- \quad (11)$$

Where  $\alpha_v$  is the vapour volume fraction,  $m^+$  and  $m^-$  represents the mass transfer rate for the vaporization and condensation processes, respectively. The sources terms are written by the following Eq:

$$m^+ = C_e \alpha_v^{\frac{2}{3}} (1 - \alpha_v)^{\frac{4}{3}} \frac{\rho_v \rho_l}{\rho_m} \sqrt{\frac{2}{3} \frac{p_v - p}{\rho_l}} \quad (12)$$

$$m^- = C_c \alpha_v^{\frac{1}{6}} (1 - \alpha_v)^2 \frac{\rho_v \rho_l}{\rho_m} \sqrt{\frac{2}{3} \frac{p - p_v}{\rho_l}}$$

With:

$$C_c = -10 R_0^{\frac{3}{2}} n_0^{\frac{5}{6}} \quad (13)$$

$$C_e = 5 \sqrt[3]{n_0} \quad (14)$$

Where  $R_0$  is the initial bubble radius,  $n_0$  is defined as nuclei concentration per unit volume of pure liquid. These two parameters are associated with the expression of the vapour volume fraction (Haosheng *et al.* 2008).

$$\alpha_v = \frac{n_0 \frac{4}{3} \pi R^3}{1 + n_0 \frac{4}{3} \pi R^3} \quad (15)$$

The value of nuclei concentration  $n_0 = 5.10^{14}$  nuclei/m<sup>3</sup><sub>water</sub> and the initial bubble radius  $R_0=5\mu\text{m}$ .

The considered cavitation model has been validated for numerous cases, such as cavitating flow around a 2D hydrofoil (Kanfoudi and Zgolli 2011; Kanfoudi 2015; Bel Hadj Taher *et al.* 2017) and 3D hydrofoil (Kanfoudi, Lamloumi, and Zgolli 2014; H. Kanfoudi *et al.* 2017).

## 2.3 Numerical Method

The simulated configuration consists of a fives impeller blades centrifugal water pump. Further performance and geometric parameters of the pump are summed up in Table 1. At first, a CAD model for the test pump was made and then discretized into a mesh. The created computational domain comprises the whole hydraulic passage of the considered centrifugal pump. So, the entire flow field can be detected and any probable asymmetrical structures are identified. The 3D view of the model pump is presented in Fig. 1. The model includes three modules: an inlet pipe portion, an impeller and thirdly a volute with an outlet duct. They are created and meshed independently. Appropriate extensions are added at the inlet and outlet to guarantee numerical stability and limit the boundary conditions consequences. Considering the configurational complexity, the mesh near the boundary is refined, as shown in Fig. 2. It brings an overview of the fluid region of the pump through the 2D grid of the whole machine (Fig.2.a) besides a close up of the 3D impeller (Fig.2.b) and volute mesh (Fig.2.c).

The accuracy and error of CFD results are attributed to the number and quality of computational grids. Since the performance prediction error will be progressively decreased with the improvement of the number of the grids; a grid sensitivity analysis based on steady simulation was performed. Thus the independence of the solutions from the number of grid nodes was inspected (Ferziger and Peric 2002).

**Table 1 Basic pump dimensions**

Parameters	value	Description
Impeller		
R <sub>i</sub>	115mm	Inlet flange radius
R <sub>1</sub>	75mm	Mean impeller inlet radius
b <sub>1</sub>	85.9mm	Inlet impeller width
β <sub>1</sub>	70°	Inlet blade angle
θ <sub>1</sub>	37°	Blade LE inclination angle
R <sub>2</sub>	204.2mm	Mean impeller outlet radius
b <sub>2</sub>	42mm	Outlet impeller width
β <sub>2</sub>	63°	Outlet blade angle
θ <sub>2</sub>	90°	Blade TE inclination angle
N <sub>a</sub>	5	Blade number
e	8mm	Blade thickness
Volute		
R <sub>3</sub>	218mm	Base volute radius
b <sub>3</sub>	20mm	Volute width
φ <sub>outlet</sub>	200mm	Outlet flange diameter
Design point		
N <sub>S</sub>	32	Specific Speed
Φ <sub>N</sub>	0.15	Nominal flow coefficient
ψ <sub>N</sub>	0.12	Nominal Head coefficient

Based on the finite volume method, a CFD code was applied to solve the governing equations for unsteady flows (3D-URANS) in the centrifugal water pump. The boundary conditions defined at the domain limits are as follows. At the inlet, a Total pressure is imposed as inflow condition and a flow rate at the outlet is defined. The no-slip boundary condition is used, on the solid walls. The impeller is set in a rotary frame with rotating speed  $\omega = 94.2$  rad/s and the other stationary parts comprising the inlet pipe and the volute casing are set in stationary frames. When steady convergence was reached, the velocity and pressure fields acquired were employed as an initialization for the unsteady flow calculations. It comprised changes in relative position between the stationary and rotating meshes. Regarding the unsteady-state simulations, the rotor-stator interactions are detected by means of the sliding mesh technique, in which an interface between the impeller and volute is created due to the rotation of the impeller. In this numerical solution, a second order scheme is employed. In order to achieve an optimal iterations number of for each time step, the convergence criterion imposed on  $10^{-5}$  must be satisfied. For the rotator passing, the time step is set  $10^{-4}$  s according to the Courant-Friedrichs-Lewy (CFL) number, which is a condition for the stability of unstable numerical methods (Courant, Lewy, and Friedrichs 1928).

$$C = V \frac{\Delta t}{\Delta x} \tag{16}$$

Where:  $V$  velocity magnitude,  $\Delta t$  is the time step and  $\Delta x$  is the length of the mesh elements.

### 3. RESULTS AND DISCUSSION

The numerical simulation in this paper aims to analyze and study the internal complex flow behaviour of a centrifugal pump on non-cavitating conditions (section 3.1) using a scale adaptive simulation. The validation of this numerical model is performed with the experimental measurement available from (Kergourlay *et al.* 2007; Coaguila 2012). Then, the modelling of the cavitation phenomenon has been treated on an isolated profile (section 3.2) which is a simpler geometry that resembles the impeller blades of a centrifugal pump. The adopted cavitation model of (Kanfoudi and Zgolli 2011) and the validation of the numerical simulation is based on the experimental results of (Leroux, Astolfi, and Billard 2004). Finally, the internal hydrodynamics of the pump considered in cavitating situations is investigated (section 3.3). The use of this cavitation model be used to predict the head drop behaviour and the effect of such phenomenon on the pump performance

#### 3.1 Flow Field Validation Under Non-Cavitating Conditions

For practical reasons, all results of the analyzed centrifugal pump are presented as dimensionless numbers: Flow coefficient ( $\phi$ ), Head coefficient ( $\psi$ ),

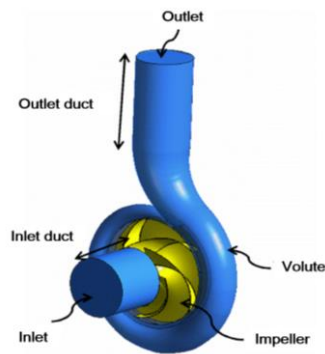


**Fig. 1. Flow simulation domain of the N<sub>s</sub> 32 pump.**

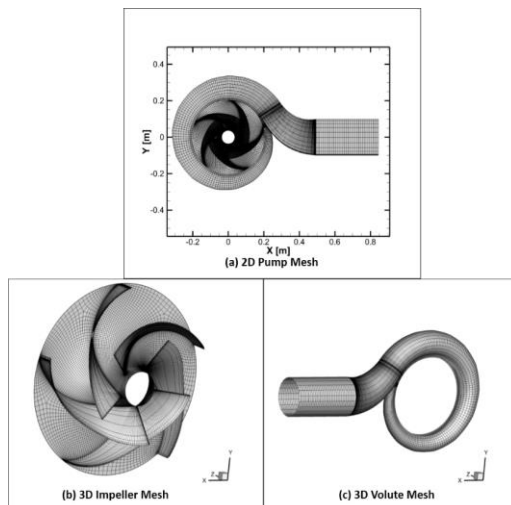


**Fig. 2. 2D Pump Mesh and 3D Meshes of the volute and impeller flow domains.**

in the following discussion and which are defined respectively as follows:

$$\phi = \frac{Q}{(\omega \cdot d_2^2 \cdot b_2)}; \psi = \frac{g \cdot H}{(\omega^2 \cdot d_2^2)} \quad (17)$$

Where  $Q$ ,  $H$ ,  $\omega$ ,  $d_2$ ,  $b_2$  and  $g$  refer to flow rate, total head, angular velocity, outlet impeller diameter, outlet impeller width and gravity respectively. We note that the total head was calculated by mass flow averaging.

The numerical results were checked first by means of comparing with experimental measurements (Coaguila 2012) of global performance characteristics and they are exposed in Fig.3. The maximal difference for the head coefficient, between the experimental and numerical results, is perceived at the highest flow rate, which reaches 16%. While the minimum difference appears at 0.12 flow rate with 1%. However, for the others flow rates, the relative error between the experimental and the numerical flow-head is equal to  $\pm 6\%$ . The maximum head coefficient prediction error was defined by:

$$e = \frac{\psi_{exp} - \psi}{\psi_{exp}} \times 100\% \quad (18)$$

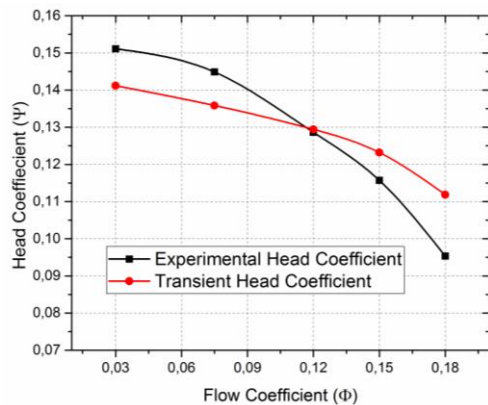


**Fig. 3. Comparison between experimental measurements and numerical results.**

Where,  $e$  is the head prediction error,  $\Psi_{exp}$  experimental head coefficient of test pump,  $\Psi$  is the head coefficient of the numerical model.

The differences between experimental and numerical results generally came from the following. Firstly, the mechanical losses like the leakage and gap losses as well as disc friction are neglected in the usual CFD set up. Secondly, the geometric discrepancies, and the uncertainty of the measurement. Thirdly, the turbulence model based on URANS, which contains many empirical parameters, cannot predict well all kinds of flow.

Besides, the pressures at the inlet and outlet of the test pump were measured by pressure sensors (Kergourlay *et al.* 2007; Coaguila 2012), whereas the numerical resolution of the pressure was calculated by an integration of the pressure

distributions on the inlet and outlet pipe section, this is also the main factor influencing the results difference. However, the deviation of the prediction head is very small, so the above CFD method can be considered as feasible and a further analysis could be carried out.

For the rest of the study, the focus will be on three flow rates named as follows:  $Q_1=0.8\Phi_N=0.12$ ;  $Q_2=\Phi_N=0.15$  and  $Q_3=1.2\Phi_N=0.18$ .

Fig.4. (a) presents the unsteady head coefficient fluctuations for the period of five rotations. Clearly, the presence of diverse wave peaks and dips can be clarified by the unsteady and complex flow field inside the pump. This is explained by the rotation of the impeller and the passage of the blades through the volute tongue. For each flow rates, it can be seen that the fluctuation amplitudes differ. We note that as the flow increases, the head coefficient fluctuations are more marked. In other words, for high flows, the flow undergoes more disturbances, which may consequently generate vibrations.

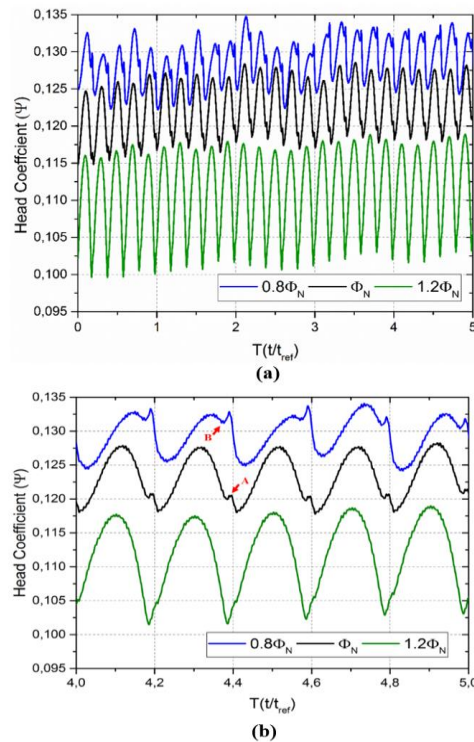


**Fig. 4. Unsteady head coefficient fluctuations for three flow rates.**

For a period matching to one wheel rotation  $t_{ref}$ , the unsteady calculation of the pump head evolution has been examined. Based on this, the average value of the last revolution was considered as the solution of the transient analysis.

The periodic fluctuating pump head plot for a simulation time covering a complete rotation of the impeller and for three flow rates is presented through Fig. 4. (b). Fluctuations generated by the motion of each blade in front of the volute tongue are clearly represented. The highest point of the head

coefficient for each flow rate indicates half a tilt of blade-to-blade rotation. The bottom of the pump head shows the entire tilt blade-to-blade rotation when the blade and the volute tongue are aligned.

For  $Q_3$ , the global head coefficient raises and decrease gradually and regularly. While the blade trailing edge is at the same line with the volute tongue, the head coefficient is at a minimum. When the volute tongue is situated between the blade-to-blade trailing edges, the head coefficient is at maximum. Nevertheless, for lower flow rates, the global head coefficient fluctuation illustrates an analogous periodic behaviour but shows supplementary information. For the nominal flow rate, the global head fluctuation illustrates a little hump after reaching the peak value. It indicates that there is strong impeller and volute tongue interaction (position A). Besides, a trough at the max level of the curve for  $Q_1$  (position B) can clearly be highlighted. It is due to the extremely unsteady flow released from the impeller exit. The deduction is: the lower the flow rate is, the more pronounced the interaction between the blade and the volute tongue is.

An additional set of inquiry was performed to verify the unsteady flow calculations. For this purpose, the numerical measures of the unsteady pressure fluctuation obtained by the CFD tool will be compared to those experimental (Kergourlay *et al.* 2007). The sensors are situated according to Figure.5 and their positions are outlined in Table 2. One sensor is placed at the front pump shroud (Cp4). Three additional sensors are set on the wall of the volute casing (Cp1, Cp2, and Cp3). The results of the numerical simulation were reported for the same positions treated in the experiments.

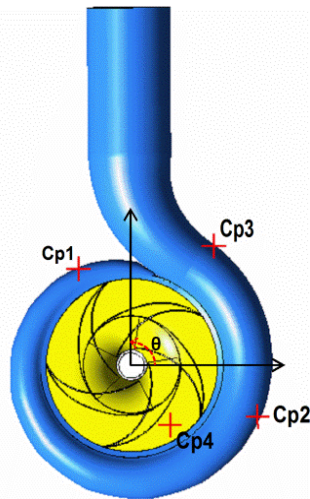


**Fig. 5. Sensors locations for blade-to-blade measurements.**

**Table 2 Sensor positions**

Sensor	Cp1	Cp2	Cp3	Cp4
Radius(mm)	On volute			168
$\theta$ (°)	120	337	60	303

As observed in Fig. 6, The experimental measures and those resulting from simulations demonstrate the passage of the five blades represented by the existence of five local maximum and minimum, recognized from the basic theory of rotor-stator interaction (Guelich and Bolleter 1992). The curves are practically periodic. This behaviour is expected considering the common effect of the flow-structure interaction between the fluid leaving the impeller and the volute tongue, on the one hand. And the local pressure variation generated by the movement of the impeller blades in front of each measurement position. (Barrio *et al.* 2011). The flow structure interaction is more pronounced nearby the tongue area, reflected by the important pressure amplitude recorded by Cp1. On the other hand, the further we get away from the zone of the volute tongue, the less the amplitude of the pressure fluctuations is important (Cp2 and Cp3).

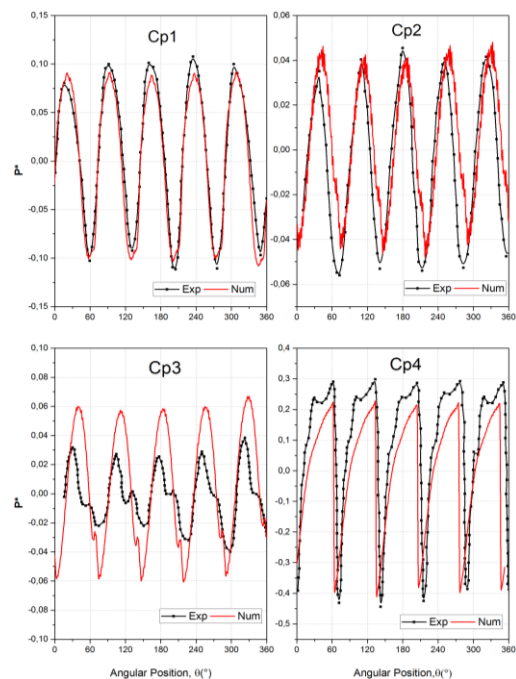


**Fig. 6. Comparisons of the numerical and experimental pressure fluctuations over one impeller revolution, ( $P^*=P-P_{ave}$ ).**

The experimental data compared to the numerical predictions presented in Fig. 6 illustrates fairly well agreement. The simulation and experimental for sensors Cp4 (on the pump front shroud), Cp1 (on the volute close to the tongue) and Cp2 (on the volute) are well predicted. Nevertheless, the result remains almost accurate for sensor Cp3 where the numerical amplitudes are overvalued. This sensor is situated near the discharge canal duct. Numerically, this position is characterized by a detached flow, which may explain the obtained results. Even if the maximum pressure amplitude is not always estimated at the identical angular location than in the experimental data, the relative error between the numerical predictions and the experimental data stands very weakly.

After validating the numerical model, the internal flow is analyzed for the three flows already presented below. To visualize the pressure fields' distribution inside the pump, Fig.7 is presented. It exposes the instantaneous static pressure contours neighbouring the confined side of the volute called the volute tongue for the three test flow rates.

A mid-plane, normal to the rotating axis of the pump, has been considered to inspect the pressure fields as well as the velocity vectors. The results were obtained when the trailing edge of the impeller blade was close to the volute tongue at a time step corresponding to  $T=t/t_{ref}=4$  ( $t=0.266s$ ). Moreover, the dynamic pressure correlated with velocity  $u_2$  normalizes the pressure  $P_{adim}$  exposed ( $P_{adim}=P/0.5.\rho.u_2^2$ ).

It can be well-noted from Fig.7, for the three flows presented, that the static pressure decreases progressively from the outer impeller periphery to the impeller eye owing to the blades impulse. Besides, for the blade-to-tongue location displayed in the actual figure, a low-pressure region can be witnessed close to the volute at design conditions, and particularly at a  $Q_1$  flow rate.

Contrariwise, a high-pressure area is perceived at this location of the pump for the  $Q_3$  flow rate. The obtained results highlighted that the mass flow rate values affect significantly the impeller volute-interaction.

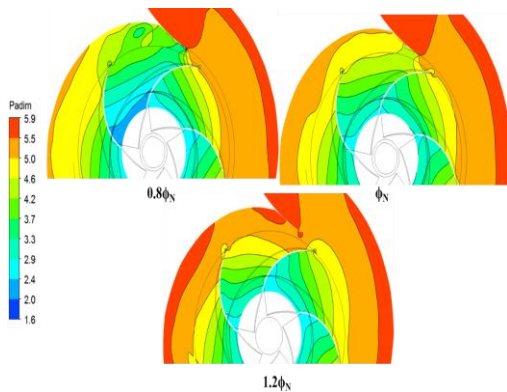


**Fig. 7. Instantaneous static pressure for three test flow rates.**

The velocity vectors near the volute tongue region are presented in Fig. 8 for the same vane position and at the same time step. Through the presented results in this figure, the effect of the flow rate on the stagnation point position on the tongue can be deduced. At design condition, the angle between the exiting fluid flow and the tongue shape are well coupled. Thereby allowing a smooth progression of the flow at mutual sides of the volute-tongue and presenting a stagnation point at its tip.

Conversely, under partial flow rate value ( $Q_1$ ), the exit angle of the fluid flow vectors differs from that at a nominal condition and noticeably disturb the flow circulation nearby the tongue. In this case, the exit angle of the flow is lower than at rated conditions and hence leads an important quantity of

the separation of the fluid from the volute. This induces a recirculation zone and a stagnation point is observed close to the volute-tongue (position A). Concerning the angle of the departing fluid at  $Q_3$ , it is clearly seen that the fluid flow vectors leave the impeller at a higher angle than that at partial and rated conditions. Therefore, the fluid flow leaves from the tight side (position B) of the volute to the large side (position C). Actually, the stagnation point is detected close to the narrow side of the volute.

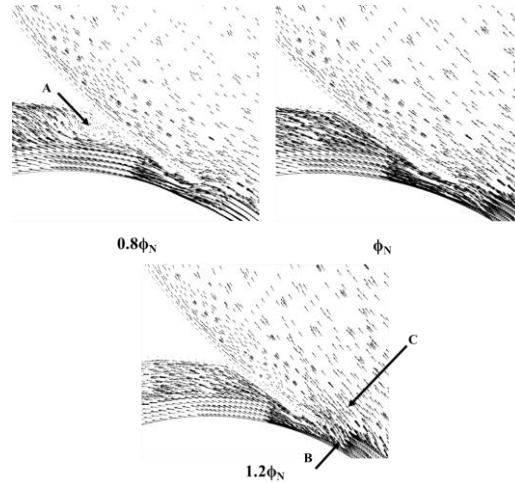


**Fig. 8. Velocity vectors at the near tongue region for three mass flow rates.**

In order to analyze the dynamic effect of the blade-tongue interaction phenomenon on the unsteady pressure field distribution, Fig. 9 reveals the instantaneous pressure distribution near-tongue region. The results were studied when operating at  $Q_1$ , at the last revolution, for the period of a one blade-passing starting at the same previous time step ( $t=0.266s$ ). The impeller is rotating in an anti-clockwise direction and a blade-passing time called  $t_{BP}$  is used to normalize the time  $t$  and the pressure by the dynamic pressure related with the tangential velocity at impeller periphery. As witnessed, the distribution of the temporal pressure field near volute tongue is significantly influenced by the relative position between the blade and the volute tongue.

At  $t/t_{BP}=0.25-0.5$ , while the rear blade of the channel is still far away from the tongue and the previous one is within the confined region of the volute, the static pressure attains maximum magnitudes. Whenever the blade trailing edge moves closer to the volute tongue for  $t/t_{BP}=0$  and 1, it is observed that the unsteady pressure diminishes. The impeller rotation induces an instantaneous unsteady pressure fluctuation localized at the impeller periphery. The pump head is consequently affected by these fluctuations.

### 3.2 Validation of the Cavitation Model Adopted

For performance evaluation of the used model, a 3D flow around a NACA 66-MOD hydrofoil is

computed to investigate the unsteady cavitation flow. A steady cavitating flow field is used as an initial condition, to increase the computation speed of the cavitation pocket.

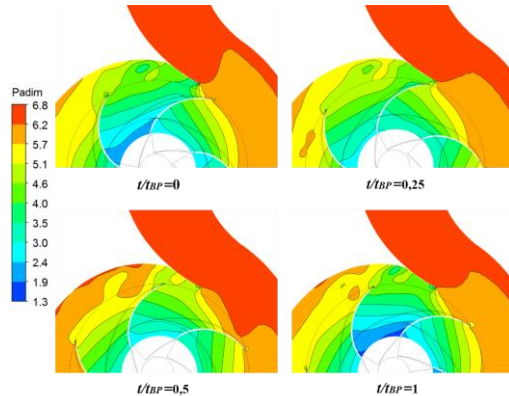


**Fig. 9. Unsteady pressure distribution along one single blade passage period (near-tongue region) at Q1.**

The hydrofoil chord was  $c = 150$  mm with a relative maximum thickness of 12% at 45% chord length from the leading edge and a relative maximum camber of 2% at 50% from the leading edge, (Leroux, Astolfi, and Billard 2004). The hydrofoil is inclined by  $6^\circ$  relative to the direction of flow.

Since the mesh topologies, has a direct repercussion on the numerical solution, a 3-D structured mesh C-grid type is applied in this investigation. To study the unsteady cavitation flow, this kind of mesh is considered as a best choice for mesh around the hydrofoil as shown in Fig.10 (a).

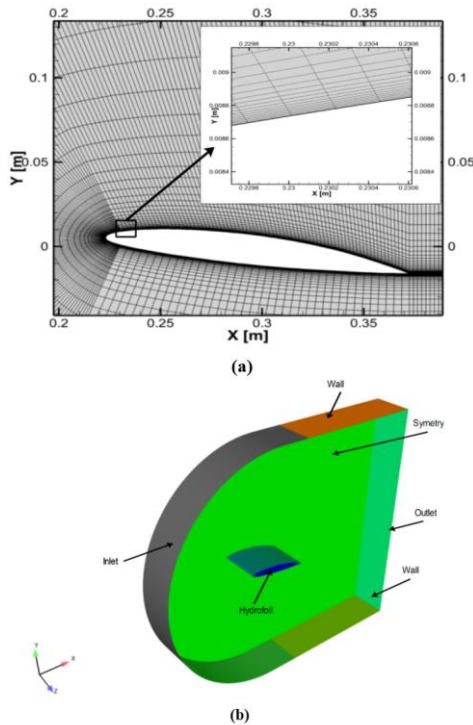


**Fig. 10. (a) Mesh spacing around NACA-66 hydrofoil, (b) Computation domain.**

The Fig. 10(b) shows the computational domain and boundary conditions. A velocity  $U = 5.33$  m/s was specified at the inflow, for the outflow, a static pressure, was introduced and calculated according to the cavitation number:

$$\sigma = (P_{out} - P_v) / \left( \frac{1}{2} \rho_l U_\infty^2 \right) \quad (19)$$

The lateral boundaries condition were set respectively, one as non-slip, the other as a periodic condition.

A Sensitivity study concerning the numerical solution of the mesh quality was conducted. Three grids with different nodes number were tested. The values of the coefficients of lift and drag in stationary flow regime were controlled as criteria of choice. Their expressions are illustrated as follows:

$$C_L = \frac{Lift}{\frac{1}{2} \rho_l U_\infty^2 c_{spanwise}} \quad (20)$$

$$C_D = \frac{Drag}{\frac{1}{2} \rho_l U_\infty^2 c_{spanwise}}$$

The below table illustrates the coefficients disparity as a function of the nodes number. Referring to the obtained results, no noticeable variation was noticed comparing the medium and the fine meshes. Therefore, the middle-resolution one was selected to simulate the unsteady cavitating flow.

**Table 3 Mesh independence test**

Mesh resolution		Cells	$C_L$	$C_D$
Mesh 1	coarse	156000	0.8912	0.0842
Mesh 2	medium	440000	0.9218	0.0855
Mesh 3	fine	1024000	0.9216	0.0854

For the calculation procedure, a time step of  $10^{-5}$  was fixed and for more accuracy of the numerical results, the criteria of convergence was based on the RMS residual type with a residual target of  $10^{-5}$ .

The validation of this numerical model is accomplished by the experimental measurement presented by (Leroux, Astolfi, and Billard 2004).

A comparison of the pressure fluctuation at five points  $x/c=0.1$ ;  $x/c=0.3$ ,  $x/c=0.5$ ;  $x/c=0.7$  and  $x/c=0.9$  from the leading edge on the suction surface along with the experimental measurement was made. Their positions are plotted in Fig.11.a. However, Fig. 11.b.c and d represents the comparison between the experimental and the numerical pressure fluctuation obtained at  $x/c = 10\%$ ,  $50\%$  and  $90\%$  from the leading edge.

As indicated in Fig. 11.b, both numerical and experimental pressure is constant around 0.03 bar, at position  $x/c=0.1$ . In this region, the cavity pocket is usually developed, which explains the pressure stabilization.

For the position  $x/c=0.5$  and  $0.9$ , the fluctuation of pressure is noticeable for two cycles. The numerical model predicts well the fluctuation of the pressure

compared to the experimental measurement. Moreover, the progressive evolution of the amplitude pressure is observed, this can be explained by the development of the re-entrant jet which causes these two signals.

By comparing experimental visualizations with the numerical results in Fig. 12, a deduction is made: the numerical model has the capacity to predict and replicate the development of the cavitation pocket through the three dimensions. Indeed, the global evolution of the computed cavity volume corresponds well with the experimental visualization.

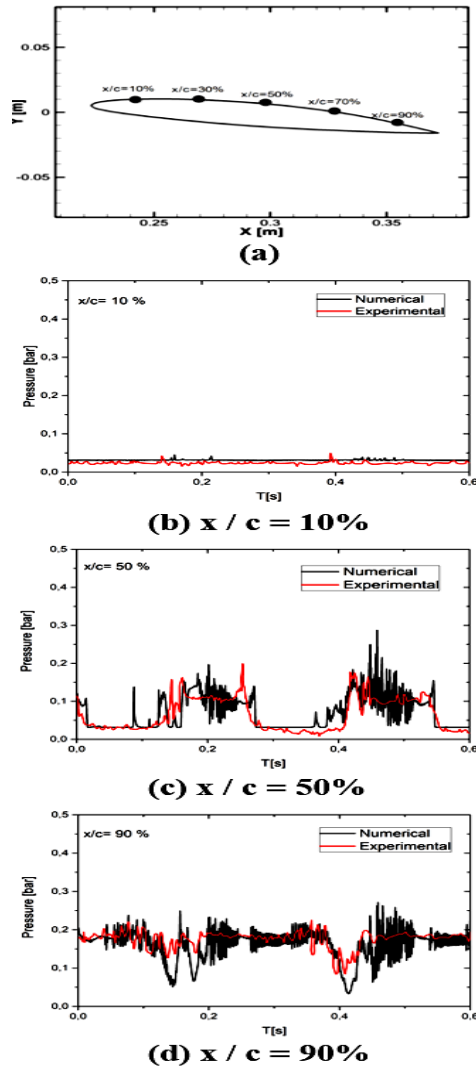


Fig. 11. (a) Localization of the point tap, (b) Comparison of the pressure fluctuation at  $x/c=10\%$ ,  $50\%$  and  $90\%$ .

Obviously, the present numerical model agrees well with the experiment particularly the pressure fluctuation measurements and the cavitation shedding dynamics. Furthermore, referring to Fig. 13, the numerical model is close to the available experimental data for the fluctuation of the lift coefficient during seven cycles. The ability of turbulence model and the cavitating model to

reproduce the cavitating behaviour is justified by this comparison.

The power spectrum density (PSD) (logarithmic scale of the y-axis) of the velocity on direction  $x$  for  $x/c=0.3$  is shown in Fig.14. The figure displays power law performance of the energy spectrum with a slope equal to  $-5/3$ . This outcome is significant. In fact, it proves that the SST-SAS turbulence model used in this investigation can capture the turbulence spectrum like LES.

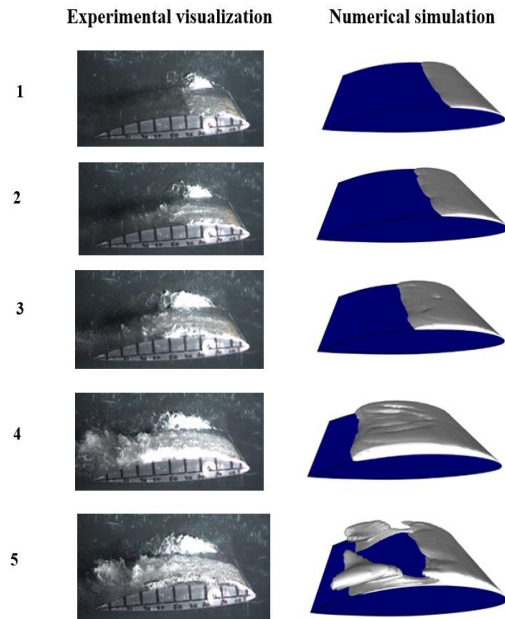


Fig. 12. Comparison of the experimental visualization (Leroux, Astolfi, and Billard 2004) and numerical simulation of the cavitation shedding.

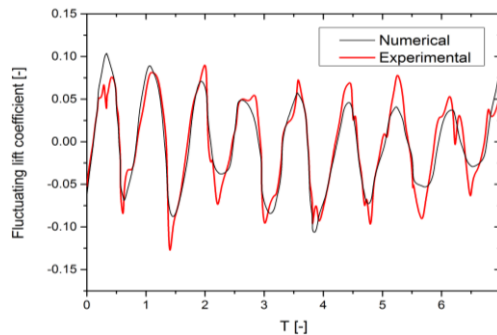
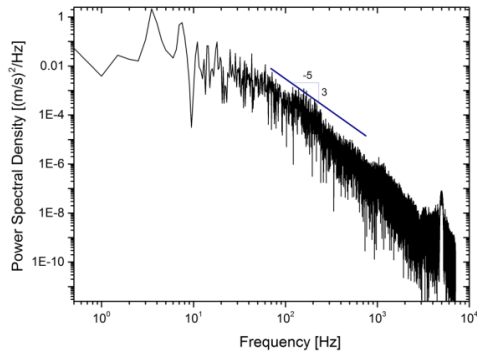


Fig. 13. Comparison of fluctuating lift coefficient.

The slope value was obtained basing on the Kolmogorov theory. This latter established the concept of universality of isotropic and locally homogenous turbulence for entirely developed turbulence at high Reynolds numbers (Davidson and Peng 2003; Peng and Haase 2008; Shur *et al.* 2008; Walters *et al.* 2013). Effectively, for a low frequency, a kinetic energy is produced and then transferred from the large structures flow. After that and for a high frequency, the large structures undergo destruction and energy dissipation then

occurs. The latter is transmitted to the new small structures which constitute the source of production of the re-entrant jet for the cavitating shedding.



**Fig. 14. Power spectrum density of velocity at  $x/c=0.3$ .**

### 3.3 Flow Field Inside the Centrifugal Pump under Cavitating Conditions

In this section, we will focus on the internal flow corresponding to the conditions of the occurrence of the cavitation phenomenon. It generally takes place when the pressure in a particular area of liquid flow falls off below the vapour pressure and, subsequently, the liquid is vaporized and occupied with the cavity.

Commonly perceived in numerous systems, such as marine propellers and hydraulic turbomachinery this phenomenon generates severe noise, vibration and erosion.

Numerical simulation of the cavitation physical characteristics of the pump was accomplished at three different flow rates and having the same rotating speed  $\omega = 94.2$  rad/s as the non-cavitating condition. The fluid temperature used for the cavitation simulation was set at  $25^\circ$ . The cavitation model presented above was used during these simulations. The cavitating unsteady calculations are very time-consuming, so we will limit ourselves, in this investigation to the stationary ones. A static pressure was set as an inlet boundary condition and a mass flow rate at the outlet was defined. Nevertheless, it should be noted that the transient calculations are underway for further future research.

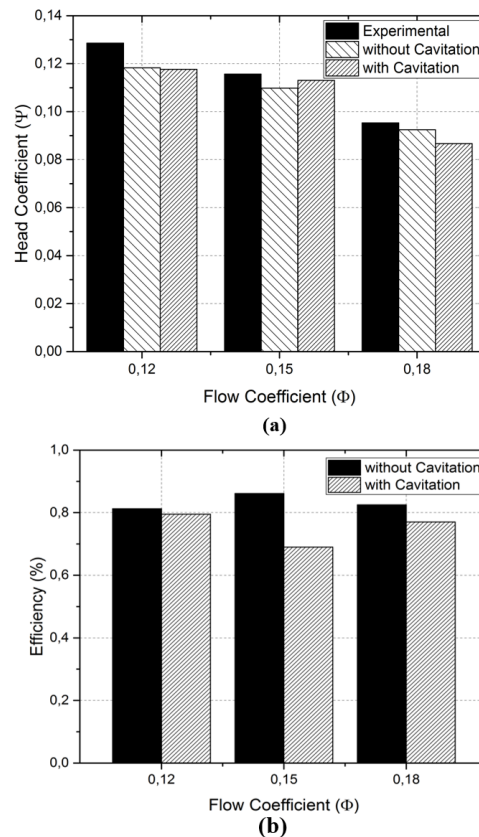
Firstly, a presentation of the elements explaining the head drop phenomenon is performed. For that, the head drop coefficient and the efficiency obtained for various flow rates are exposed. And next, the cavity evolution is examined.

Fig. 15.a illustrates the comparison of pump head coefficient between the experimental and numerical results, in non-cavitating and cavitating conditions.

For the three cases, the value of the head in the cavitating case is lower than the experimental one. This can be explained by the appearance of a vapour cavity which affected the pump normal flow and then decreased the pump head. However, for the nominal rate, the cavitating head coefficient is much

closer to the experimental value in comparison to the non-cavitating one. As a matter of fact, this proves the existence of a vapour pocket even if the pump works in design conditions.

To examine the effect of considering the cavitation phenomenon, the efficiency has been calculated and shown in Figure 15.b. As it can be seen, a drop in performance is remarkable through the reduction of the efficiency of the pump and more particularly for the nominal flow rate. In fact, and as explained above, the presence of the cavity disorders the flow through the pump impeller channels by acting as an obstacle. Consequently, a reduction in performance and efficiency is observed.



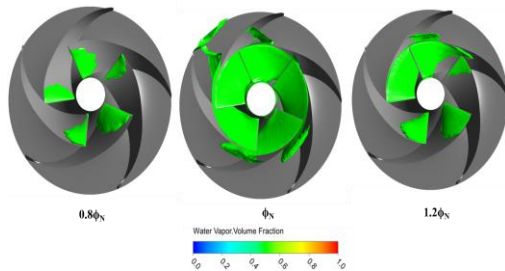
**Fig. 15. Comparison of: (a) pump head coefficient between calculation and experiment; (b) pump efficiency with and without cavitation.**

Fig. 16 shows the cavity development in the impeller for the three flow rates ( $Q_1$ ,  $Q_2$ , and  $Q_3$ ), so that the 3D shape and spread of the cavity can be assessed. A representation of the iso-surface of  $\alpha = 0.6$  is illustrated. Naturally, this is merely a qualitative evaluation of the cavity boundary, as one can select another iso-surface as the cavity boundary.

The cavity inception and development in the pump are clearly obtained. The vapour pocket was situated in the rotor. In the volute there was no vapour for the investigated flow rates.

Under partial flow rate,  $Q_1$  the cavity appears only on the suction side near the blade leading edge. With the increase of the flow coefficient, the vapour

pockets firstly occur near the leading edge of the rotor blade and then gradually developing. Hence, the pump flow will be affected, and the head of the pump starts to fall. However, the vapour distribution through the blades is not uniform, as shown for the highest flow rate Q3. The pocket cavity is greater on the blades close to the volute tongue and more particularly on the one whose trailing edge is just at the level of the tongue. This shows the effect of the interaction between the rotor and the stator on the cavitation pocket.



**Fig. 16. Development of cavitation in the impeller for ( $0.8 \Phi_N$ ,  $\Phi_N$ , and  $1.2 \Phi_N$ ).**

At nominal conditions, the impeller channels seem to be more obstructed by the cavities, which results in the pump efficiency decline. The cavity arises initially on the suction side and then develops mainly in a radial direction until reaching the half of the five blades, which incites the performance drop. Lastly, cavitation develops on pressure side very close to the shroud (Luo, Ji, and Tsujimoto 2016).

#### 4. CONCLUSION

The present article mainly focuses, in his first part, on the unsteady flow field behaviour within a centrifugal pump on non cavitating conditions. The use of the SST-SAS (Scale Adaptive Simulation) turbulence model leads to a satisfactory consistency between the experiments and the numerical results. The numerical unsteady head coefficients propose reasonable approximations with an acceptable accuracy.

The transient head coefficient curves display a periodic fluctuation; however, the fluctuation amplitudes are not the same, which is mostly produced by the unsteadiness of the flow field inside the pump. We deduced that the interaction between the blade and the volute tongue is more pronounced for the lower flow rate. Furthermore, the unsteady pressure fluctuation inside the impeller and at the volute casing wall was calculated. The comparison of the numerical results acquired with the available experimental results shows a satisfactory agreement. Once the numerical model has been validated, a temporal analysis of the unsteady pressure and velocity fields' distribution was studied for three different flow rates.

Additionally, the unsteady cavitating flow around a NACA66-MOD hydrofoil was numerically

inspected. The experimentally observed cavitating flow features are well replicated by the numerical model results. This investigation showed that turbulence model coupled with the Kanfoudi cavitation model was able to reproduce in 3D the cavitating behaviour and the evolution of the vapour pocket.

Afterwards, a focus has been done on the prediction of the appearance of the cavitation phenomenon as well as its impact on the performances of the pump. For the three flow rates investigated, a decrease in performance through the head and efficiency drop is observed. In fact, the obtained steady values were lower than the experimental ones, mainly at design conditions. The appearance of the cavity of vapour disturbed the pump flow through the impeller channels and then reduced the pump head. It can be seen that the vapour pocket developed only in the rotor and arises initially on the suction side nearby the blade leading edge. It has also been noticed that the cavity on the blades neighboring the volute tongue, mainly on the one whose trailing edge is just at the level of the tongue is greater.

#### REFERENCES

- Akhras, A., M. El Hajem, J. Y. Champagne and R. Morel (2004). The Flow Rate Influence on the Interaction of a Radial Pump Impeller and the Diffuser. *International Journal of Rotating Machinery*. 10 (4), 309–317.
- Al-Qutub, A., A. Khalifa and Y. Khulief (2009). Experimental Investigation of the Effect of Radial Gap and Impeller Blade Exit on Flow-Induced Vibration at the Blade-Passing Frequency in a Centrifugal Pump. *International Journal of Rotating Machinery*. 1–10.
- Asuaje, M., F. Bakir, S. Kouidri, F. Kenyery and R. Rey (2005). Numerical Modelization of the Flow in Centrifugal Pump: Volute Influence in Velocity and Pressure Fields. *International Journal of RotatingMachinery*. 3, 244–55.
- Bakir, F., S. Kouidri, T. Belamri and R. Rey (2001). On a General Method of Unsteady Potential Calculation Applied to Compression Stages of a Turbomachine-Part I: Theoretical Approach. *Journal of fluids engineering*. 780–86.
- Barre, S. J. Rolland, G. Boitel, E. Goncalves and R. Fortes Patella (2009). Experiments and Modelling of Cavitating FLOws in Venturi: Attached Sheet Cavitation. *European Journal of Mechanics B/Fluids*. 28 (1), 444–64.
- Barrio, R., J. Fernandez, E. Blanco and J. Parrondo (2011). Estimation of Radial Load in Centrifugal Pumps Using Computational Fluid Dynamics. *European Journal of Mechanics, B/Fluids*. 30 (3) ,316–24.
- Barrio, R., J. Parrondo and E. Blanco (2010). Numerical Analysis of the Unsteady Flow in the Near-Tongue Region in a Volute-Type Centrifugal Pump for Different Operating

- Points. *Computers and Fluids*. 39 (5), 859–70.
- Bel Hadj Taher, A., H. Kanfoudi, M. Ennouri, R. Zgolli (2017). Numerical Study of Unsteady Cavitating Flows around a Hydrofoil. *Journal of Applied Fluid Mechanics* 10 (1), 447–58.
- Brennen, Christopher E. (2011). *Hydrodynamics of Pumps*.
- Cheah, K. W., T. S. Lee and S. H. Winoto (2008) Unsteady Fluid Flow Study in a Centrifugal Pump by CFD Method. *7th Asean ANSYS Conference*, Biopolis, Singapore.
- Coaguila, M. S. S. (2012). *Analyse Numérique et Expérimentale Des Fluctuations de Pression Dans Les Pompes Centrifuges*. Ph. D. thesis, L'École Nationale Supérieure d'Arts et Métiers, Paris, France
- Courant, R., H. Lewy and K. Friedrichs (1928). Über Die Partiellen Differenzgleichungen Der Mathematischen Physik. *Mathematische Annalen / Mathematische* 43, 32–74.
- Coutier-Delgosha, O., P. Morel, R. Fortes Patella and J. L. Reboud (2005). Numerical Simulation of Turbopump Inducer Cavitating Behavior. *International Journal of Rotating Machinery*. (2), 135–42.
- Coutier-Delgosha, O., J. L. Reboud, Y. Dellanoy and Y. Delannoy (2003). Numerical Simulation of the Unsteady Behaviour of Cavitating Flows. *International Journal for Numerical Methods for Fluids*. 42 (5), 527–48.
- Croba, D. and J. L. Kueny (1996). Numerical calculation of 2D, unsteady flow in centrifugal pumps: impeller and volute interaction. *International Journal for Numerical Methods in Fluids*. 22 (6), 467–81.
- Davidson, L. and S. H. Peng (2003). Hybrid LES-RANS Modelling: A One-Equation SGS Model Combined with a  $k-\omega$  Model for Predicting Recirculating Flows. *International Journal for Numerical Methods in Fluids*. 43 (9), 1003–18.
- Deshpande, M., J. Feng and C. L. Merkle (1994). Cavity Flow Predictions Based on the Euler Equations. *Journal of fluids engineering*. 116, 36–44.
- Dong, R., S. Chu and J. Katz (1997). Effect of Modification to Tongue and Impeller Geometry on Unsteady Flow, Pressure Fluctuations, and Noise in a Centrifugal Pump. *Journal of Turbomachinery*. 119, 506–15.
- Dong, R. and J. Katz (1995). Relationship Between Unsteady Flow, Pressure Fluctuations, and Noise in a Centrifugal Pump — Part B: Effects of Blade-Tongue Interactions. *Journal of Fluids Engineering*. 117: 24–29.
- Feng, J., F. K. Benra and H. J. Dohmen (2009). Comparison of Periodic Flow Fields in a Radial Pump among CFD, PIV, and LDV Results. *International Journal of Rotating Machinery*.
- Ferziger, J. H. and M. Peric (2002). *Computational Methods for Fluid Dynamics*. Springer-Verlag, Berlin.
- González, J. and C. Santolaria (2006). Unsteady Flow Structure and Global Variables in a Centrifugal Pump. *Journal of Fluids Engineering* 128 (5), 937.
- Guelich, J. F. and U. Bolleter (1992). Pressure Pulsations in Centrifugal Pumps. *Journal of vibration and acoustics*. 114, 272–279.
- Haosheng, C., L. Jiang, L. Fengbin, C. Darong and W. Jiadao (2008). Experimental Study of Cavitation Damage on Hydrogen-Terminated and Oxygen-Terminated Diamond Film Surfaces. *Wear*. 264(1–2), 146–151.
- Hosono, K., Y. Kajie, S. Saito, and K. Miyagawa (2015). Study on Cavitation Influence for Pump Head in an Axial Flow Pump. *Journal of Physics: Conference Series* 656.
- Kanfoudi, H., G. Bellakhal, M. Ennouri, A. Bel Hadj Taher and R. Zgolli (2017). Numerical Analysis of the Turbulent Flow Structure Induced by the Cavitation Shedding Using LES. *Journal of Applied Fluid Mechanics*. 10(3), 933–46.
- Kanfoudi, H. (2015). Modeling and Computation of the Cavitating Flow in Injection Nozzle Holes. *International Journal of Modeling, Simulation, and Scientific Computing*. 06(01).
- Kanfoudi, H., H. Lamoumi and R. Zgolli (2012). Numerical Investigation for Steady and Unsteady Cavitating Flows. *Advances in Modeling of Fluid Dynamics*. 87–96.
- Kanfoudi, H., H. Lamoumi and R. Zgolli (2014). Modelling of Unsteady Cavitating Flow. *International Journal of Renewable Energy Technology*. 5(2), 20–22.
- Kanfoudi, H. and R. Zgolli (2011). A Numerical Model To Simulate the Cavitating Flows. *International Journal of Modeling, Simulation, and Scientific Computing*. 2(3), 277–97.
- Kergourlay, G., M. Younsi, F. Bakir and R. Rey (2007). Influence of Splitter Blades on the Flow Field of a Centrifugal Pump: Test-Analysis Comparison. *International Journal of Rotating Machinery*.
- Kitano, M. and Siekmann H. E. (2000). Numerical Calculation of Secondary Flow in Pump Volute. *International Journal of Rotating Machinery* 6(4), 245–52.
- Koop, A. H. (2008). *Numerical Simulation of Unsteady Three-Dimensional Sheet Cavitation*.
- Kozubková, M., J. Rautová and M. Bojko (2012). Mathematical Model of Cavitation and Modelling of Fluid Flow in Cone. *Procedia Engineering*. 39(1), 9–18.
- Kubota, A., H. Kato and H. Yamaguchi (1992). A

- New Modelling of Cavitating Flows: A Numerical Study of Unsteady Cavitation on a Hydrofoil Section. *Journal of Fluid Mechanics*. 240(1), 59.
- Laberteaux, K. R. and S. L. Ceccio (2001). Partial Cavity Flows. Part 1. Cavities Forming on Models without Spanwise Variation. *Journal of Fluid Mechanics*. 431, 1–41..
- Lamloumi, H., H. Kanfoudi and R. Zgolli (2012). Numerical simulation of cavitation flow in turbomachine. In *International Symposium on Multiphase Flow and Transport Phenomena*.
- Lauder, B. E. and D. B. Spalding (1974). The Numerical Computation of Turbulent Flows. *Computer Methods in Applied Mechanics and Engineering*. 3(2),269–89..
- Lei, T., Z. H. U. Baoshan, C. A. O. Shuliang and W. Yuming (2013). Cavitation Flow Simulation for a Centrifugal Pump at a Low Flow Rate. *Chinese Science Bulletin*. 58 (8), 949–52.
- Lei, T., Z. B. Shan, C. S. Liang, W. Y. Chuan and W. Bin Bin (2013). Numerical Simulation of Unsteady Cavitation Flow in a Centrifugal Pump at Off-Design Conditions. *J Mechanical Engineering Science*. 1–13.
- Leroux, J. B., J. A. Astolfi and J. Yv. Billard (2004). An Experimental Study of Unsteady Partial Cavitation. *Journal of Fluids Engineering*. 126(1), 94.
- Li, W. G. (2014). Validating Full Cavitation Model With an Experimental Centrifugal Pump. *TASK Quarterly*. 18 (1), 81–100.
- Liu, H. L., D. X. Liu, Y. Wang, X. F. Wu and J. Wang (2013). Application of Modified  $\kappa\text{-}\omega$  Model to Predicting Cavitating Flow in Centrifugal Pump. *Water. Science and Engineering*. 6(3),331–39.
- Liu, H. L., J. Wang, Y. Wang, H. Zhang and H. Huang. (2014). Influence of the Empirical Coefficients of Cavitation Model on Predicting Cavitating Flow in the Centrifugal Pump. *International Journal of Naval Architecture and Ocean Engineering*. 6(1), 119–31.
- Li, G., Y. Wangl, P. Caol, Y. Cul and G. Yinl (2013). Numerical analysis of transient flow in centrifugal pump at off-design conditions.
- Longatte, F. and J. L. Kueny (1999). Analysis of Rotor-Stator-Circuit Interactions in a Centrifugal Pump. *Proceedings of the 3 Rd ASME/JSME Joint Fluids Engineering Conference*. 9(9), 1–7.
- Luo, X-w., B. Ji and Y. Tsujimoto (2016). A Review of Cavitation in Hydraulic Machinery. *Journal of Hydrodynamics* 28(3), 335–58.
- Majidi, K. (2015). Numerical Study of Unsteady Flow in a Centrifugal Pump. *Journal of Turbomachinery*.
- Maxime, B. and F. C. Li (2016). Numerical Study and Analysis of Cavitation Performance in Centrifugal Impellers Numerical Study and Analysis of Cavitation Performance in Centrifugal Impellers. *International Journal of Engineering and Technical Research* 4, 552-556.
- Maxime, B. and F.C. Li (2016). Centrifugal pump performance and cavitation effects-a review.
- Meng, G., L. Tan, S.L. Cao, W. Jian, W.W. Liu and D. J. Jiang (2014). Numerical Simulation and Analysis of Cavitation Flows in a Double Suction Centrifugal Pump. *International Symposium of Cavitation and Multiphase Flow*.
- Meng, L., M. He, L. Zhou, J. Yang, Z. Wang and B. Karney (2016). Influence of Impeller-Tongue Interaction on the Unsteady Cavitation Behavior in a Centrifugal Pump Long. *Engineering Computations*. 33(1), 171–83.
- Menter, F. R. and Y. Egorov (2010). The Scale-Adaptive Simulation Method for Unsteady Turbulent Flow Predictions. Part 1: Theory and Model Description. *Flow, Turbulence and Combustion*. 85 (1), 113–38.
- Menter, F. R. (1994). Two-Equation Eddy-Viscosity Turbulence Models for Engineering Applications. *AIAA Journal*. 32(8), 1598–1605.
- Parrondo Gayo, J. L., J. Gonzalez Perez and J. Fernandez-Francos (2002). The Effect of the Operating Point on the Pressure Fluctuations at the Blade Passage Frequency in the Volute of a Centrifugal Pump. *Journal of Fluids Engineering* 124(3), 784-790.
- Pavesi, G., G. Cavazzini and G. Ardizzon (2008). Time-Frequency Characterization of Rotating Instabilities in a Centrifugal Pump with a Vaned Diffuser. *International Journal of Rotating Machinery*. 2008.
- Peng, S.H. and W. Haase (2007). Advances in Hybrid RANS-LES Modelling. In *2007 Symposium on Hybrid RANS-LES Methods*, 331. Corfu, Greece.
- Pouffay, B., R. Fortes-Patella, J. L. Reboud and P. A. Lambert (2005). Numerical simulation of 3d cavitating flows: analysis of cavitation head drop in turbomachinery. In *FEDSM2005-77356*, 1–9.
- Sauer, J. and G. H. Schnerr (2000). Unsteady Cavitating Flow: A New Cavitation Model Based on a Modified Front Capturing Method and Bubble Dynamics. *Proceedings of 2000 ASME Fluid Engineering Summer Conference*. 11–15.
- Senocak, I. and W. Shyy (2004). Interfacial Dynamics Based Modelling of Turbulent Cavitating Flows, Part 1: Model Development and Steady State Computations. *International Journal for Numerical Methods in Fluids*. 995,975–95.

- Shojaeefard, M. H., M. Tahani, A. Khalkhali, M. B. Ehghaghi, H. Fallah and M. Beglari (2013). A Parametric Study for Improving the Centrifugal Pump Impeller for Use in Viscous Fluid Pumping. *Heat and Mass Transfer/Waerme-Und Stoffuebertragung*. 49(2), 197–206..
- Shuai, Z.J., C.X. Jiang, D.H. Wang, Z.H. Zhou and F.C. Li (2015). Numerical Simulation of Dynamic Flow Characteristics in a Centrifugal Water Pump with Three-Vaned Diffuser. *Advances in Mechanical Engineering*. 7 (8).
- Shur, M.L., P.R. Spalart, M. K. Strelets and A K. Travin (2008). A Hybrid RANS-LES Approach with Delayed-DES and Wall-Modelled LES Capabilities. *International Journal of Heat and Fluid Flow*. 29(6), 638–49.
- Singhal, A. K., M. M. Athavale, H. Li and Y. Jiang (2002). Mathematical Basis and Validation of the Full Cavitation Model. *Journal of Fluids Engineering*. 124(3): 617.
- Song, P., Y. Zhang, C. Xu, X. Zhou and J. Zhang. (2015). Numerical Studies on Cavitation Behavior in Impeller of Centrifugal Pump with Different Blade Profiles. *International Journal of Fluid Machinery and Systems*. 8(2), 94–101.
- Tan, L., S.L. Cao, Y. M. Wang, B. S. Zhu, T. Lei, C. A. O. Shuliang, W. Yuming and Z. H. U. Baoshan (2012). Influence of Axial Distance on Pre-Whirl Regulation by the Inlet Guide Vanes for a Centrifugal Pump. *Science China Technological Sciences*. 55(4), 1037–43.
- Tan, L., B. Zhu, Y. Wang, S. Cao and S.Gui (2015). Numerical Study on Characteristics of Unsteady Flow in a Centrifugal Pump Volute at Partial Load Condition. *Engineering Computations (Swansea, Wales)*. 32(6), 1549–66.
- Walters, D. K., S. Bhushan, M. F. Alam and D. S. Thompson (2013). Investigation of a Dynamic Hybrid RANS/LES Modelling Methodology for Finite-Volume CFD Simulations. *Flow, Turbulence and Combustion*. 91(3), 643–67.
- Wang, Xi. and D. Li (2014). Application of Scale Adaptive Simulation Based on K- $\Omega$  SST Turbulence Model. In *29th Congress of the International Council of the Aeronautical Sciences*.
- Winkler, C.M. and A.J. Dorgan (2011). Scale Adaptive Simulations of Turbulent Flows on Unstructured Grids. 1–36.
- Wu, J., Y. Utturkar and W. Shyy (2003). Assessment of modeling strategies for cavitating flow around a hydrofoil. In *Fifth International Symposium on Cavitation*. 1–8.
- Wu, J., G. Wang and W. Shyy (2005). Time Dependent Turbulent Cavitating Ow Computations with Interfacial Transport and Ylter-Based Models. *Int. J. Numer. Meth. Fluids* 49, 739–761.
- Xu, Y., Y. Chen, D. Homa, W. Wróblewski, Y. Xu and Y. Chen (2014). Modelling of Flow with Cavitation in Centrifugal Pump. *Journal of Physics: Conference Series*. 530, 012032.
- Yuan, W., J. Sauer and G. H. Schnerr (2001). Modeling and Computation of Unsteady Cavitation Flows in Injection. *Nozzles. Mecanique et Industries*. 2(5), 383–94.
- Yulin, W., L. Shuhong and S. Jie (2009). Numerical Simulation on the Steady and Unsteady Internal Flows of a Centrifugal Pump. In *Numerical Simulations Examples and Applications in Computational Fluid Dynamics*.
- Zhang, N., M. Yang, B. Gao, Z. Li and D. Ni (2015). Experimental Investigation on Unsteady Pressure Pulsation in a Centrifugal Pump With Special Slope Volute. *Journal of Fluids Engineering*. 137.
- Zwart, P., A. Gerber and T. Belamri (2004). A Two-Phase Flow Model for Predicting Cavitation Dynamics. *Fifth International Conference on Multiphase Flow, Yokohama, Japan*.